Inorganic Chemistry

Article

pubs.acs.org/IC

Synthesis, Crystal Structure, and Transport Properties of the Hexagonal Mo_9 Cluster Compound $Ag_3RbMo_9Se_{11}$

Patrick Gougeon,*[,†] Philippe Gall,[†] Odile Merdrignac-Conanec,[†] Lionel Aranda,[‡] Anne Dauscher,[‡] Christophe Candolfi,[‡] and Bertrand Lenoir[‡]

[†]Institut des Sciences Chimiques de Rennes, UMR 6226 CNRS−Université de Rennes 1−INSA de Rennes, 11 allée de Beaulieu, CS 50837, 35708 Rennes Cedex, France

[‡]Institut Jean Lamour, UMR 7198 CNRS−Université de Lorraine, Parc de Saurupt, CS 50840, 54011 Nancy, France

ABSTRACT: Mo-based cluster compounds are promising candidates for thermoelectric applications at high temperatures due to their very low lattice thermal conductivity values. Here, we report on a detailed investigation of the crystal structure and transport properties measured in a wide range of temperatures (2−800 K) of polycrystalline $Ag_3RbMo_9Se_{11}$. Single-crystal X-ray diffraction shows that this compound crystallizes in the hexagonal space group $P6_3/m$. The crystal structure is formed by stacked Mo_9Se_{11} units leaving channels that are randomly filled by Rb^+ cations, while Ag^+ cations are located between the Mo_9Se_{11} units. The high disorder in the unit cell induced by these atoms and their large anisotropic thermal displacement parameters are two key characteristics that lead to very low lattice thermal conductivity as low as 0.6 W m^{-1} K^{-1} at 800 K. The combination of semiconducting-like electrical properties and low ability to transport heat leads to a maximum dimensionless thermoelectric figure of merit ZT of 0.4 at 800 K.

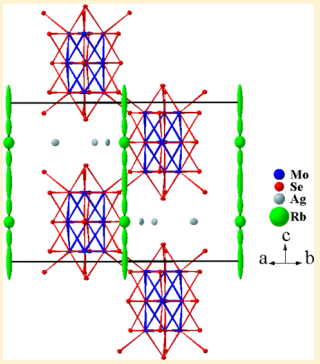

INTRODUCTION

Thermoelectric materials possess the remarkable ability to directly convert heat into electrical current and vice versa, offering many prospects in waste-heat energy recovering.[1−3] Yet, a broad use of this technology has so far been prevented due to the low conversion efficiency reached in state-of-the-art thermoelectric compounds.[1−3] The thermoelectric efficiency is determined by the dimensionless figure of merit $ZT = \alpha^2 T/\rho(\kappa_L + \kappa_e)$.[1−3] High ZT materials should exhibit, at a given absolute temperature T, a high thermopower α, a low electrical resistivity ρ, and low lattice (κ_L) and electronic thermal conductivity (κ_e). Hence, the crystal structure of an ideal thermoelectric material should show crystallographic features scattering efficiently acoustic phonons but without being at the expense of the mobility of the charge carriers. This unusual and conflicting combination of transport properties makes the design of such a material a complex challenge.

Mo-based cluster compounds provide a particularly interesting area of research to find novel compounds that show intrinsically very low lattice thermal conductivity values of ∼0.5 W m^{-1} K^{-1} above room temperature.[4−9] In addition to being nearly optimized with respect to the thermal transport, these phases offer several degrees of freedom to tune their electrical properties including the size and geometry of Mo clusters as well as the rich variety of elements that can be inserted in the voids left by the three-dimensional arrangement of these clusters.[10−16] Among the phases recently studied, our initial works on the transport properties of the $Ag_xMo_9Se_{11}$ ($3.4 \leq x \leq 3.8$) compounds revealed promising thermoelectric properties at 800 K that primarily stem from their very low lattice thermal conductivity that nears the glassy limit at 800 K (0.5 W m^{-1} K^{-1}).[4,5] The origin of this amorphous-like heat transport is tied to the large voids located between the $Mo_9Se^i_{11}Se^a_6$ bi-octahedral clusters (where i and a stand for innen and außen, respectively, according to Schäfer's notation[28]), where Ag^+ cations are distributed over four independent crystallographic sites and exhibit large anisotropic thermal displacement parameters.[4,5,17] This remarkable property results in a maximum ZT of 0.65 at 800 K reached at the maximum Ag filling level of $x = 3.8$.[4]

We recently investigated the possibility to further tune the carrier concentration of these compounds through substitutions on the Se site by either S or Te.[18] Relative to the pristine sample, the increased metallic character of the electronic transport did not yield enhanced ZT values. Furthermore, the low solubility limit of both chalcogen atoms suggests that the Mo−Se clusters are less flexible to substitutions than the Ag sites are. Our prior studies with Tl and Cu partially replacing Ag have shown that good thermoelectric properties could be obtained at high temperatures with ZT values of ∼0.6 at 800 K for the Tl and Cu compounds.[6,19] Of note, such substitutions can also result in different structure types as exemplified by the Tl-containing compound $Ag_2Tl_2Mo_9Se_{11}$ crystallizing in the trigonal space group $R\bar{3}c$ and for which bi-octahedral Mo_9 units are connected to six neighboring cluster units.[6] Another example of this polymorphism is provided by the alkali element Cs, which leads to the hexagonal compound $Ag_{2.6}CsMo_9Se_{11}$ (space group $P6_3/m$).[20] Its crystal structure also contains $Mo_9Se^i_{11}Se^a_6$ bi-octahedral cluster units that form tunnels

Received: May 11, 2017

DOI: 10.1021/acs.inorgchem.7b01200
Inorg. Chem. XXXX, XXX, XXX−XXX

running along the [001] direction, where the Cs cations reside. The Ag^+ cations occupy statistically 6h sites in the mirror planes around the ternary axis between two adjacent Mo_9Se_{11} units.

Here, we report on the novel compound $Ag_3RbMo_9Se_{11}$ that crystallizes isostructurally to $Ag_{2.6}CsMo_9Se_{11}$. We explored its electrical and thermal properties in a wide temperature range (5−800 K) and show that this compound exhibits semiconducting-like electrical properties and very low thermal conductivity values that remain well under 1 W m^{-1} K^{-1} between 5 and 800 K, yielding a maximum ZT value of 0.4 at 800 K.

EXPERIMENTAL SECTION

Syntheses and Densification. All the elemental powders were stored and manipulated in an argon-filled, dry glovebox. The synthesis of $Ag_3RbMo_9Se_{11}$ was realized by using powders of the precursors $MoSe_2$ and $Rb_2Mo_6Se_6$ mixed with elemental Ag and Mo powders. Mo powder was heated under H_2 flowing gas at 1273 K for 10 h to eliminate possible traces of oxygen. The $MoSe_2$ precursor was synthesized by direct reaction of Mo and Se in stoichiometric proportions placed in an evacuated silica tube at 973 K for 48 h. The $Rb_2Mo_6Se_6$ precursor was synthesized in two steps. First, the ternary compound $In_2Mo_6Se_6$ was prepared by heating a mixture of InSe, $MoSe_2$, and Mo powders in stoichiometric proportions at 1273 K during 36 h in an evacuated silica tube. The second step consisted in an ion-exchange reaction of $In_2Mo_6Se_6$ with RbCl at 1073 K. For this purpose, $In_2Mo_6Se_6$ and RbCl powders were mixed in the proportion of 1:2.5 and subsequently cold-pressed. The cylindrical pellet was introduced in a long silica ampule sealed under vacuum. The end of the ampule, where the pellet was placed, was introduced in a furnace, heated at 1073 K during 2 d, while keeping the other end of the tube at room temperature. All these starting compounds were single-phase according to their laboratory powder X-ray diffraction patterns. At 1473 K, single-phase powders of $Ag_{3-x}RbMo_9Se_{11}$ were observed for $0 \leq x \leq 0.4$. Note that, here, we restricted our transport property investigation to the $x = 0.0$ compound.

The resulting polycrystalline pellets of $Ag_3RbMo_9Se_{11}$ were finely ground and densified by hot uniaxial pressing (HUP) realized under a residual argon pressure (~1 × 10^{-2} mbar). A quantity of ~5 g of $Ag_3RbMo_9Se_{11}$ was introduced into a graphite crucible (Ø = 12 mm) that was before coated with boron nitride. The pressure was applied from the beginning of the temperature increase (8 °C/min) to the end of the high-temperature dwell of 2 h at 1473 K. The applied load was 50 MPa at the beginning of the heating and was gradually augmented up to 85 MPa when the temperature of 1473 K was obtained. The experimental density was determined from the dimensions and weight of the pellet and was ~98% of its theoretical value.

Single-Crystal and Powder X-ray Diffraction (PXRD). Measurements were performed with a Nonius Kappa CCD diffractometer using Mo Kα radiation (λ = 0.710 73 Å) on a small single crystal obtained by heating a powder of $Ag_3RbMo_9Se_{11}$ to 1573 K, at which temperature the latter compound begins to decompose. An absorption correction (T_{min} = 0.1121, T_{max} = 0.2754) based on the crystal shape was used.[21] Structure solution and full matrix least-squares refinements were performed using the Sir97 and SHELX softwares, respectively.[22,23] After refinement of the Mo−Se framework, a subsequent difference-Fourier synthesis reveals the presence of Ag atoms and a quasi-continuous electron density along the c axis due to the Rb atoms (Figure 1). The latter was modeled with three partly occupied rubidium sites using second-order tensors for the anisotropic displacement parameters. Anharmonic treatment of the rubidium atoms using the program JANA2000[24] was unsuccessful. The final occupation factors for the Ag atoms were refined freely. Analysis of the intensity data using the TwinRotMat routine of PLATON[25] revealed the studied crystal was twinned by merohedry with [100, −1−10, 00−1] as the twin matrix. The ratio of the twin components was refined to 0.0175(6):0.9825(6), which lowered the R factor from 0.0425 to 0.0321. The relevant parameters of the data collection and structure refinement are listed in Table 1. The refined crystallographic parameters and selected interatomic distances are given in Tables 2

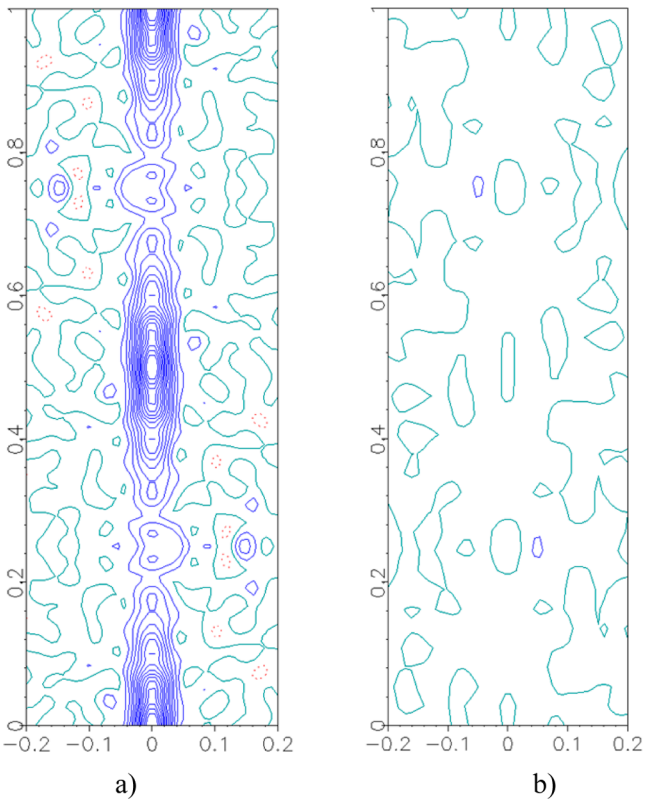

Figure 1. Fourier difference maps along the c axis in $Ag_{2.6}RbMo_9Se_{11}$ (a) after refinement of the Mo−Se framework (step: 2 e $Å^{-3}$) and (b) after the final refinement.

Table 1. Relevant Parameters of the Single-Crystal Data Collection and Structure Refinement of $Ag_{2.6}RbMo_9Se_{11}$

empirical formula	$Ag_{2.6}RbMo_9Se_{11}$
molar mass (g mol^{-1})	2098.49
temperature	293(2) K
symmetry	hexagonal
space group	$P6_3/m$
a (Å)	10.0384(2)
c (Å)	11.9930(2)
V ($Å^3$)	1046.62(5)
Z	2
ρ (g·cm^{-3})	6.659
crystal size (mm^3)	0.08 × 0.07 × 0.06
radiation	Mo Kα (0.710 69 Å)
θ range (deg)	1.698−34.989
absorption coefficient (mm^{-1})	28.991
limiting indices	$-16 \leq h \leq 12$, $-10 \leq k \leq 16$, $-19 \leq l \leq 19$
reflection collected/unique	14 329/1604
refinement method	full-matrix least-squares on F^2
data/parameters	1604/53
final R indices [$I > 2\sigma(I)$]	$R1$ = 0.0321, $wR2$ = 0.0724
R indices (all data)	$R1$ = 0.0399, $wR2$ = 0.0753
extinction coefficient	0.000 48(9)
largest diff. peak and hole (e·$Å^{-3}$)	1.859 and −1.618
goodness-of-fit on F^2	1.159

DOI: 10.1021/acs.inorgchem.7b01200
Inorg. Chem. XXXX, XXX, XXX−XXX

Table 2. Fractional Atomic Coordinates, Equivalent Isotropic Displacement Parameters (Å^2), Wyckoff Positions, and Site Occupancy Factors (s.o.f.) for $Ag_{2.6}RbMo_9Se_{11}$

atom	x	y	z	U_{eq} (Å^2)	Wyckoff	s.o.f.
Mo1	0.176 52(4)	0.522 75(4)	0.564 10(3)	0.010 01(9)	12i	1
Mo2	0.179 87(6)	0.674 82(6)	0.7500	0.009 50(11)	6h	1
Se1	0.047 81(6)	0.695 86(6)	0.565 33(4)	0.013 04(11)	12i	1
Se2	0.028 78(8)	0.377 73(8)	0.7500	0.013 04(14)	6h	1
Se3	0.3333	0.6667	0.106 77(7)	0.014 27(16)	4f	1
Ag1	−0.257 35(9)	0.144 72(9)	0.7500	0.0278(2)	6h	0.869(4)
Rb1	0.0000	0.0000	−0.150(7)	0.08(2)	4e	0.065(9)
Rb2	0.0000	0.0000	0.2500	0.080(8)	2a	0.152(13)
Rb3	0.0000	0.0000	0.0000	0.280(18)	2b	0.718(17)

and 3, respectively. More details on the crystal structure study can be obtained from the Fachinformationszentrum Karlsruhe, 76344 Eggenstein-Leopoldshafen, Germany, (fax: (49) 7247−808−666; e-mail: crysdata@fiz.karlsruhe.de) on quoting the depository number CSD-433045.

Table 3. Main Interatomic Distances (Å) for $Ag_{2.6}RbMo_9Se_{11}$, $Ag_{2.6}CsMo_9Se_{11}$, and *h*-Mo_9Se_{11}

distances	$Ag_{2.6}RbMo_9Se_{11}$	$Ag_{2.6}Cs_{2.6}Mo_9Se_{11}$	*h*-Mo_9Se_{11}
Mo(1)−Mo(1)	2.6216(7)	2.6270(4)	2.6820(6)
Mo(1)−Mo(2)	2.6928(5)	2.6937(4)	2.7370(4)
Mo(1)−Mo(2)	2.7376(5)	2.7365(4)	2.7985(5
Mo(2)−Mo(2)	2.7419(10)	2.7423(6)	2.6838(9)
Mo(1)−Se(3)	2.5475(8)	2.5439(5)	2.5234(7)
Mo(1)−Se(1)	2.6034(6)	2.6035(7)	2.5909(6)
Mo(1)−Se(1)	2.6334(6)	2.6328(6)	2.6000(6)
Mo(1)−Se(2)	2.6703(5)	2.6683(3)	2.7026(5)
Mo(1)−Se(1)	2.7120(6)	2.7130(4)	2.6090(6)
Mo(2)−Se(2)	2.5829(9)	2.5808(6)	2.5672(8)
Mo(2)−Se(2)	2.5853(9)	2.5902(5)	2.5893(8)
Mo(2)−Se(1) (×2)	2.6433(6)	2.6408(5)	2.5357(5)
Ag(1)−Se(2)	2.6463(10)	2.6408(5)	
Ag(1)−Se(1) (×2)	2.7760(7)	2.7935(5)	
Ag(1)−Se(3) (×2)	2.9261(9)	2.8719(7)	
Rb(1)−Se(1) (×3)	3.47(2)		
Rb(1)−Se(2) (×3)	3.85(3)		
Rb(2)−Se(2) (×3)	3.6560(7)		
Rb(2)−Se(1) (×6)	3.9902(5)		
Rb(3)−Se(1) (×6)	3.4104(5)		

PXRD data were collected on bulk pieces ground into fine powders and placed on a zero-background Si sample holder. The data were collected at 300 K with a Bruker D8 Advance diffractometer with Cu Kα_1 radiation (λ = 1.540 56 Å). Refinements were performed with the Fullprof and Jana2000 software.[24,26]

Scanning Electron Microscopy (SEM). SEM experiments were performed to unveil possible secondary phases, the concentration of which is below the detection limit of PXRD. Images were collected on polished surfaces of bulk pieces in the backscattering electron (BSE) mode using a Quanta 650 FEG (FEI). Corresponding X-ray elemental maps were taken to determine the distribution of the elements within the sample.

Thermogravimetry and Differential Scanning Calorimetry (TG−DSC). Bulk pieces of the dense pellets were used for TG−DSC analysis. Data were collected using a TG−DSC 92−16.18 apparatus (Setaram). A sample of ∼48 mg was loaded into an alumina crucible. The thermal response of the sample was monitored between 300 and 800 K under an argon flow with a constant low heating rate of 2 K min^{-1} to obtain a good thermal coupling between the sample and the crucible.

Low-Temperature Transport Properties. Bar-shapes and disks were cut from the consolidated pellet with a diamond-wire saw for transport property measurements. Electrical resistivity, thermopower, and thermal conductivity were measured simultaneously between 5 and 300 K on bar-shaped samples (∼1.5 × 1.5 × 8 mm^3) using the thermal transport option (TTO) of a physical property measurement system (PPMS, Quantum Design). Electrical and thermal contacts were realized by gluing four copper bars with conducting silver epoxy. Hall effect measurements were performed at selected temperatures between 5 and 300 K and under magnetic fields ranging between −1 and +1 T. The measurements were performed using a five-probe method with the alternating current (AC) transport option of the PPMS. The electrical contacts were realized by attaching copper wires onto the samples using a small amount of silver paste. Specific heat was measured from 300 to 2 K by a conventional relaxation method using the PPMS. The sample of ∼15 mg was glued onto the sample holder by a minute amount of Apiezon N grease.

High-Temperature Transport Properties. A ZEM-3 apparatus (Ulvac-Riko) was used to measure simultaneously the electrical resistivity and thermopower between 300 and 800 K on bar-shaped samples (∼1.5 × 1.5 × 8 mm^3). The thermal conductivity was determined between 300 and 800 K through thermal diffusivity (a) measurements using a laser flash instrument (LFA 467, Netzsch). These measurements were conducted on disk-shaped samples (∼12 mm in diameter, ∼1 mm in thickness) spray-coated with graphite prior to measurements to obtain a homogeneous signal absorption and emission. Both quantities are related via the relation $\kappa = \alpha C_P d$, where C_P is the specific heat, and d is the density. C_P was evaluated using the Dulong−Petit law ($C_P = 3NR$ in which N is the number of atoms per formula unit, and R is the gas constant) and, hence, was considered temperature-independent in the covered temperature range. Here, we neglected the temperature dependence of the density. Longitudinal and transverse sound velocities were measured at 300 K on disk-shaped sample using a pulse-echo method. We utilize honey to ensure a good coupling between the sample and the ultrasonic transducers.

RESULTS AND DISCUSSION

Crystal Structure. The crystal structure was successfully refined on a single crystal with the final composition $Ag_{2.6}RbMo_9Se_{11}$ in the hexagonal space group $P6_3/m$. The substoichiometry in Ag stems from the higher temperature (1573 K) used during the crystal-growth process, which led to a loss of silver as observed by the formation of silver droplets at the top of the tube. The Mo−Se network results from interlinked Mo_9Se_{11} clusters via Mo−Se bonds (Figure 2a). The Mo_9Se_{11} unit has the point symmetry C_{3h} and can be viewed as resulting from the uniaxial face-sharing of two Mo_6Se_8 units after removal of the Se atoms capping the shared faces. Alternatively, the Mo_9Se_{11} can be viewed as the superposition of three quasi-planar Mo_3Se_3 in staggered position, instead of two in Mo_6Se_8 clusters, with two additional Se atoms capping the outer triangular faces. The Mo−Mo and Mo−Se bond

DOI: 10.1021/acs.inorgchem.7b01200
Inorg. Chem. XXXX, XXX, XXX−XXX

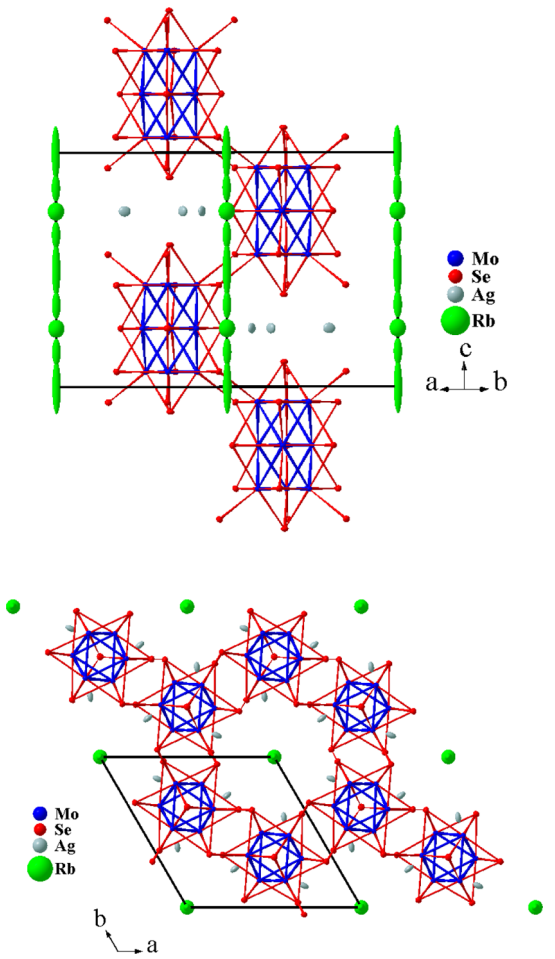

Figure 2. (upper) Crystal structure of the $Ag_3RbMo_9Se_{11}$ in perspective view. (lower) Projection of the crystal structure along the (001) plane (the thermal ellipsoids are drawn at the 50% probability level).

lengths, shown in Table 3, are very close in the two isomorphous compounds $Ag_{2.6}RbMo_9Se_{11}$ and $Ag_{2.6}CsMo_9Se_{11}$ but differ significantly from those determined in the empty variant *h*-Mo_9Se_{11}. The similarity of the Mo−Mo distances reflects faithfully the identical metallic electron count (MEC); that is, electrons available for metal−metal bonding, equal to 35.6 in both compounds, while in the binary compound, the MEC is only 32. This is also confirmed by the average distances Mo−Mo in the Mo_9 cluster that are 2.6922(4) and 2.6938(4) in $Ag_{2.6}RbMo_9Se_{11}$ and $Ag_{2.6}CsMo_9Se_{11}$, respectively, and 2.7313(7) in the binary. All these observations agree well with previous studies that showed that any change in the MEC induces variations of the Mo−Mo distances in the Mo_9 cluster.[20,27] The connective formula of the molybdenum−selenium framework is $[Mo_9Se_5{}^{i}Se_{6/2}{}^{i\text{-}a}]Se_{6/2}{}^{a\text{-}i}$ according to the notation of Schäfer.[28] As shown by the Figure 2b showing the projection of the crystal structure of $Ag_{2.6}RbMo_9Se_{11}$ onto the (a,b) plane, large hexagonal tunnels that are randomly filled by the Rb^+ cations run along the *c*-axis. The Ag^+ cations occupy partially positions in the mirror planes around the ternary axes between adjacent Mo_9Se_{11} units located on the threefold axes. Its Se environment can be seen as a distorted square pyramid with Ag−Se bond lengths ranging from 2.6463(10) to 2.9261(9) Å (Figure 3). The Rb2 cations are in distorted tricapped trigonal prismatic selenium environment, while the

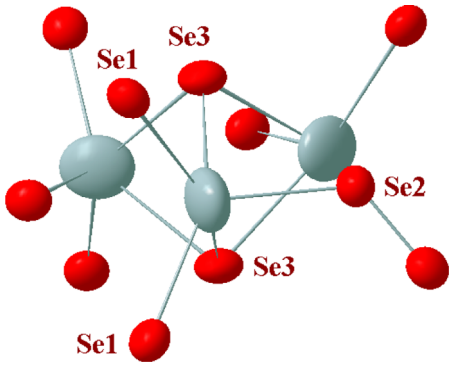

Figure 3. Selenium environments of the Ag atoms (the thermal ellipsoids are drawn at the 97% probability level).

Rb1 and Rb3 are each surrounded by six Se atoms forming flattened octahedra along the ternary axis. The Rb−Se distances spread over a wide range, 3.4104 (5)−3.9902 (5) Å. Both the Ag and Rb sites are partially occupied, introducing strong positional disorder in the unit cell. As in other Mo cluster chalcogenides,[4−12] the Ag and particularly the Rb atoms exhibit large anisotropic thermal displacement parameters (Table 2) that likely give rise to low-energy features in the phonon spectrum as observed, for instance, in clathrates or tetrahedrites.[29−36]

Phase Characterization and Thermal Stability. The PXRD pattern of $Ag_3RbMo_9Se_{11}$ refined in profile matching method is shown in Figure 4. According to this analysis, the

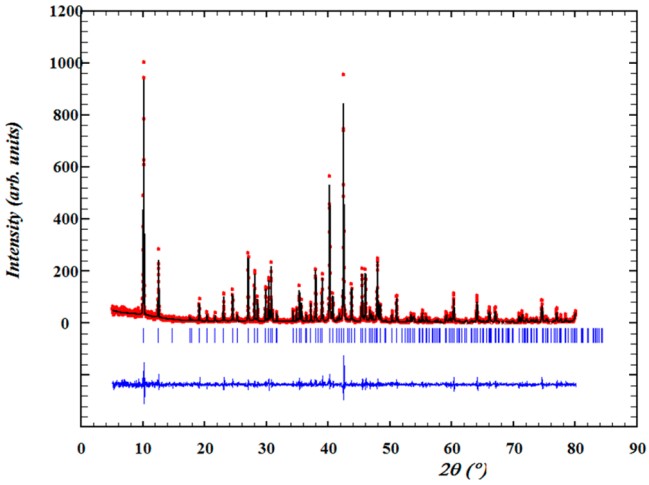

Figure 4. Profile matching method refinement of the PXRD pattern for polycrystalline $Ag_3RbMo_9Se_{11}$. The experimental data are shown in red, while the overlaid solid black line corresponds to the calculated profile. The difference profile between the theoretical and experimental patterns is shown in blue. The vertical blue ticks stand for the Bragg reflections.

polycrystalline sample was found single-phase. On the one hand, as is often the case in chalcogenides with molybdenum clusters exhibiting cationic disorders, the refinement in Rietveld method has not yielded very reliable results. However, we could deduce the composition $Ag_{3.1}Rb_{1.3}Mo_9Se_{11}$. On the other hand, the silver atom occupying a position 6h, the stoichiometry in silver cannot exceed 3, and the cationic charge cannot be greater than +4 (i.e., 36 electrons per Mo_9 cluster), we can conclude that the stoichiometry of the synthesized powder is

DOI: 10.1021/acs.inorgchem.7b01200
Inorg. Chem. XXXX, XXX, XXX−XXX

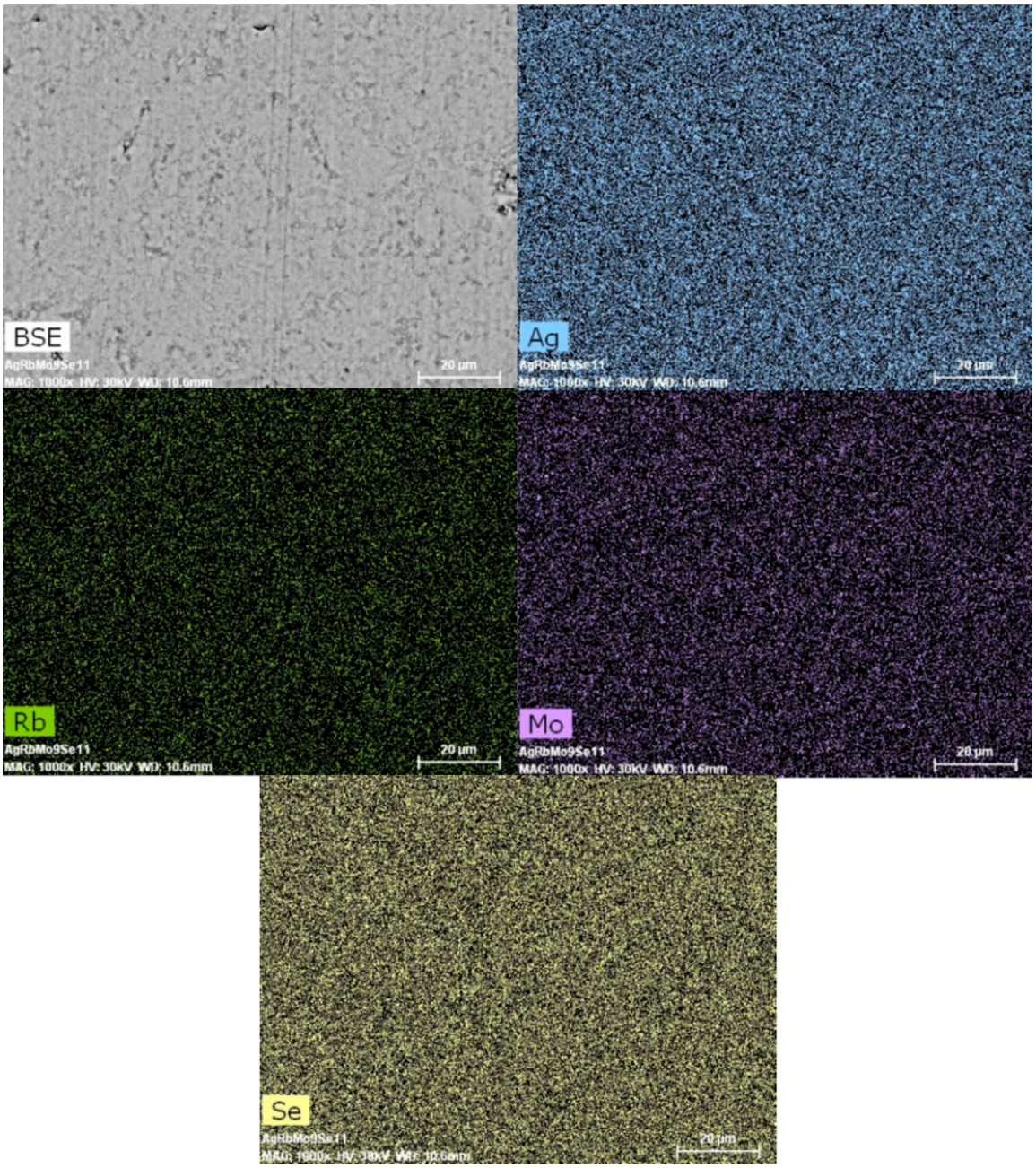

Figure 5. BSE images and corresponding elemental X-ray maps of the consolidated polycrystalline sample used for transport properties measurements.

very close to $Ag_3RbMo_9Se_{11}$. This is also confirmed by the elemental mappings along with the backscattered electron images (Figure 5), collected on a piece of the consolidated sample, which confirm the absence of secondary phases indicating that no thermal decomposition occurred during the HUP process. The chemical composition, estimated by energy-dispersive electron spectroscopy (EDXS) to be $Ag_{2.9}Rb_{1.1}Mo_{9.2}Se_{11}$ (normalized to 11 Se atoms per chemical formula), is close to the nominal composition. The X-ray elemental maps indicate a homogeneous distribution of all the elements.

According to the TG–DSC analysis shown in Figure 6, $Ag_3RbMo_9Se_{11}$ does not exhibit any sign of thermal decomposition or phase transition in the temperature range covered. No endothermal or exothermal event is observed in the DSC curve up to 800 K. The small mass increase observed in the TG curve upon heating (~1.5% at 800 K) is likely due to slight surface oxidation during data collection.

Electronic Transport Properties. The evolution of the electrical properties with the chemical compositions of compounds containing Mo cluster units can be rationalized by the MEC. Density functional theory (DFT) calculations have shown that the MEC is equal to 32 electrons for the structural motif Mo_9Se_{11}, while a count of 36 is required to reach a semiconducting state.[37] These additional electrons are provided by the elements inserted in the large channels of the crystal structure assuming ionic interactions between these cations and the Mo–Se clusters. For instance, in the $Ag_xMo_9Se_{11}$ phase, a semiconducting state is predicted for x = 4 supposing that the Ag atoms exhibit an oxidation state of

DOI: 10.1021/acs.inorgchem.7b01200
Inorg. Chem. XXXX, XXX, XXX–XXX

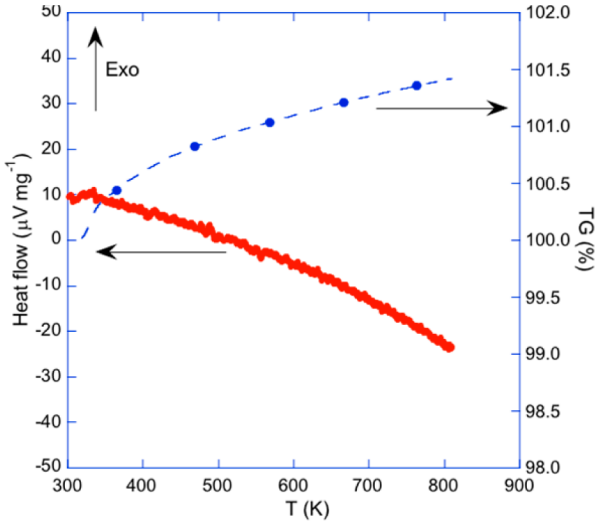

Figure 6. TG–DSC traces for polycrystalline $Ag_3RbMo_9Se_{11}$. The solid and dashed curves correspond to DSC and TG, respectively.

+1. Although a semiconducting state is not reached in these compounds due to the maximum Ag filling level of $x = 3.8$, the overall variations of the electrical properties are in agreement with this simple picture.[4,5] Considering the similarity between the crystal structures of $Ag_{2.6}RbMo_9Se_{11}$ and $Ag_{2.6}CsMo_9Se_{11}$, the electronic structure of $Ag_{2.6}RbMo_9Se_{11}$ should be very similar to the one of the cesium analogue. Previously, density functional calculations were performed on the model compound $Ag_3CsMo_9Se_{11}$.[20] These calculations showed that, for an MEC of 36 electrons, the Mo–Mo bonding and nonbonding bands are separated from the Mo–Mo antibonding bands by a band gap of ~1 eV.[20] Because of the ionic interaction between the alkaline and the Mo–Se clusters, the nature of the alkaline metal and its position in the channel hardly perturb the electronic structure of $Ag_3MMo_9Se_{11}$ (M = Rb, Cs). Therefore, we can anticipate that $Ag_3RbMo_9Se_{11}$ should be close to a semiconducting state as well, assuming that Ag and Rb are both in a +1 state. The variations in the electrical resistivity and thermopower as a function of temperature, shown in Figure 7a,b, respectively, are consistent with this prediction. $\rho(T)$ follows an activated behavior, indicative of a semiconducting character. As most of the Mo-based cluster compounds studied so far, α is positive in the investigated temperature range, suggestive of holes as the dominant charge carriers. This behavior is consistent with a Fermi level hosted in the top of the valence bands. As shown in Figure 7b, $\alpha(T)$ increases nearly linearly to 560 K. Above this temperature, the slope of $\alpha(T)$ is significantly lower, and α reaches a maximum of ~150 μ V/K at 800 K. This variation in the slope of $\alpha(T)$ at high temperatures has also been observed in the cluster compound $Ag_2Tl_2Mo_9Se_{11}$.[6] The TG–DSC analysis did not evidence any obvious thermal events around 560 K suggesting that this behavior might be purely electronic in origin and related to modifications in the balance between the electron and hole contributions to α.

Thermal Transport Properties. The temperature dependence of the specific heat C_P is depicted in Figure 8a. Near 300 K, C_P approaches the Dulong–Petit value of $3NR$. The $C_P(T)$ data follow a conventional Fermi-liquid dependence $C_P = \gamma T + \beta T^3$only at very low temperatures. A fit of the $C_P(T)$ data following this relation confirms the semiconducting ground state of $Ag_3RbMo_9Se_{11}$, synonymous with a null electronic contribution $\gamma(T)$ to within experimental uncertainty. The phonon contribution characterized by the parameter β leads to a very low Debye temperature of 130 K. This value is consistent with those inferred in other cluster compounds.[4−8]

In cagelike materials such as clathrates,[29−33] the low-energy excitations associated with the encaged atoms that exhibit the largest atomic displacement parameters (ADP) give rise to additional contributions to the specific heat at low temperatures. This excess specific heat is usually evidenced as a pronounced peak in the C_P data plotted as C_P/T^3 versus T that can be adequately modeled by Einstein oscillators.[29−33] Mo-based cluster compounds feature similar contributions associated with the thermal vibrations of the cations located in the intercluster voids. $Ag_3RbMo_9Se_{11}$ provides another example of a system with low-energy excitations as reflected by the peak visible in the C_P/T^3 (T) data (Figure 8b) at ~3 K. Yet, a detailed analysis based on Einstein oscillators in these compounds is less straightforward due to a more complex low-energy phonon spectrum than in clathrates.

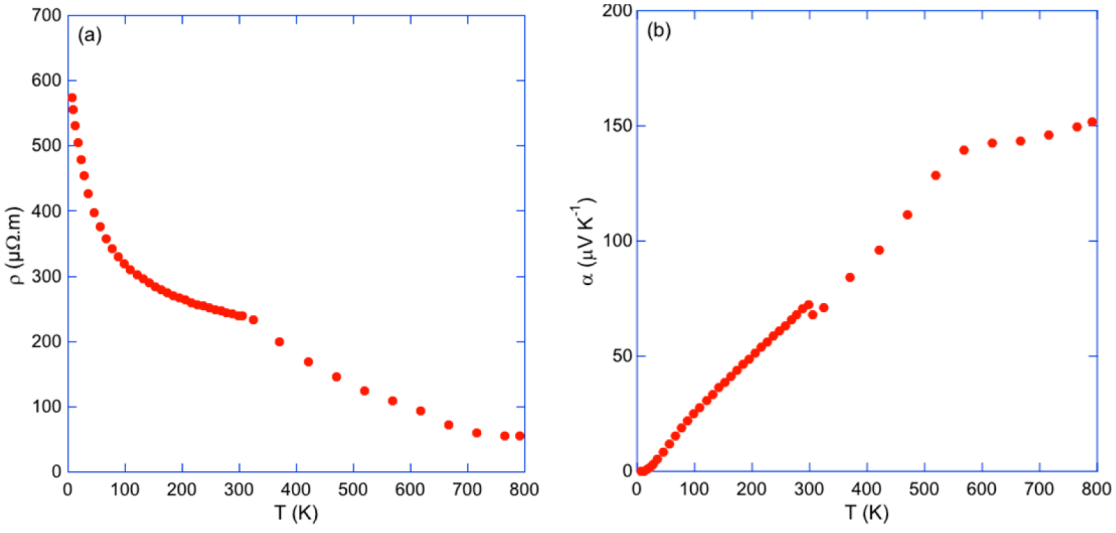

Figure 7. Temperature dependence of the electrical resistivity ρ (a) and thermopower α (b) for $Ag_3RbMo_9Se_{11}$.

DOI: 10.1021/acs.inorgchem.7b01200
Inorg. Chem. XXXX, XXX, XXX–XXX

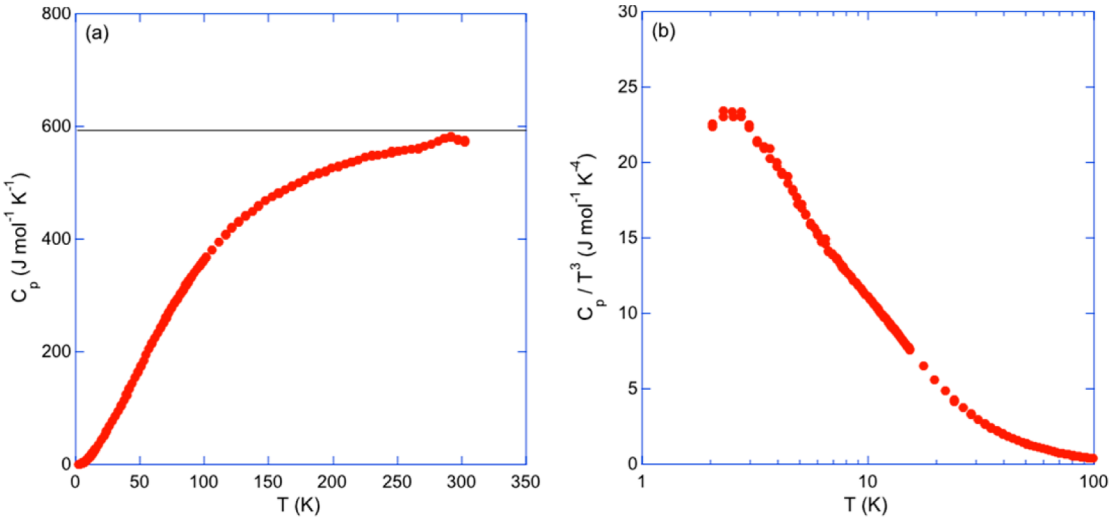

Figure 8. (a) Specific heat C_P as a function of temperature. The horizontal black solid line corresponds to the Dulong–Petit value. (b) Specific heat data plotted as C_P/T^3 vs T to visualize the low-temperature peak associated with the presence of low-energy excitations.

These characteristics are likely important ingredients that are at the origin of the very low thermal conductivity κ values (Figure 9) that remain well below 1 W m^{-1} K^{-1} between 5 and

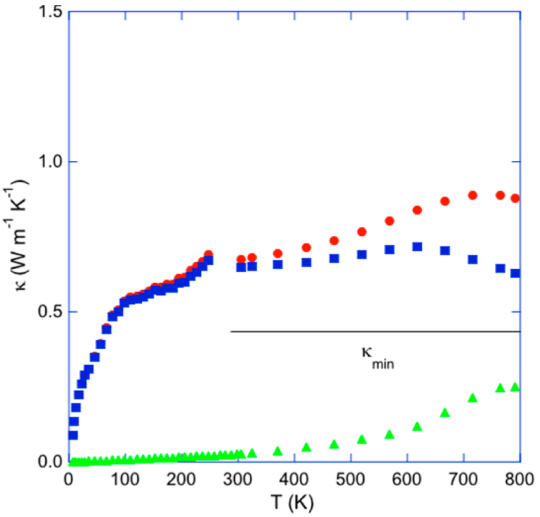

Figure 9. Total (red ●), electronic (green ▲), and lattice (blue ■) thermal conductivity as a function of temperature for $Ag_3RbMo_9Se_{11}$. The lack of data between 250 and 300 K and the slight upturn observed above 200 K are due to thermal radiations that accompany the low-temperature measurements. The solid black line represents the theoretical minimum of the lattice thermal conductivity κ_{min}.

800 K. The electronic thermal conductivity κ_e was estimated using the Wiedemann–Franz law $\kappa_e = LT/\rho$, where L is the Lorenz number. The variations in temperature of L were approximated by a single-parabolic-band model. While below 300 K $\kappa \approx \kappa_L$due to the high ρ values, κ_e reaches ~30% of the total thermal conductivity at 800 K. κ_L slightly diminishes when the temperature increases to reach ~0.6 W m^{-1} K^{-1} at 800 K. At high temperatures, these values are close to the minimum lattice thermal conductivity which can be calculated above the Debye temperature from $\kappa_{min} = \frac{1}{2}\left(\frac{\pi}{6}\right)^{1/3} k_B V^{-2/3}(2\nu_T + \nu_L)$where V is the average volume per atom in the unit cell, and ν_T and ν_L are the experimental transverse and longitudinal sound velocities, respectively.[38] With ν_T = 1347 m/s and ν_L = 3287 m/s, this formula yields $\kappa_{min} \approx$ 0.43 W m^{-1} K^{-1}. This compound thus makes no exception to the general fact that Mo-based cluster compounds feature very low lattice thermal conductivity, a property that tends to be practically independent of the size and geometry of the clusters and of their spatial distribution within the unit cell.

Dimensionless Thermoelectric Figure of Merit. The temperature dependence of the ZT values is shown in Figure 10. Despite the low thermal conductivity values, the rather large

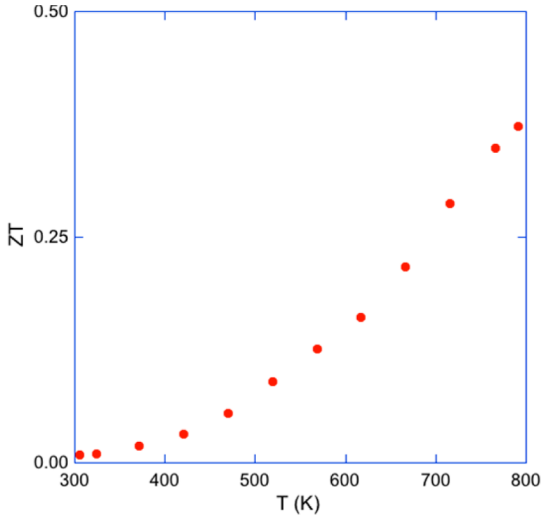

Figure 10. Temperature dependence of the dimensionless figure of merit ZT for $Ag_3RbMo_9Se_{11}$.

electrical resistivity values lead to a moderate ZT of 0.4 at 800 K. Investigations of S and Te substitutions for Se in the sister compound $Ag_{3.8}Mo_9Se_{11}$ have shown that both elements reinforce the metallic character of the electronic conduction.[18] Hence, further optimization of the power factor of $Ag_3RbMo_9Se_{11}$ through these isovalent substitutions on the Se sites might help to tune the electrical resistivity.

DOI: 10.1021/acs.inorgchem.7b01200
Inorg. Chem. XXXX, XXX, XXX–XXX

CONCLUSION

We reported on the successful synthesis of the $Ag_3RbMo_9Se_{11}$ cluster compound. Single-crystal X-ray diffraction measurements performed at 300 K evidenced the high disorder induced by the Ag and Rb ions, both of them showing large ADP values. Within the temperature range of 300−800 K, the title compound is stable with no signs of phase transitions or mass loss. $Ag_3RbMo_9Se_{11}$ shows very low thermal conductivity values (0.7 W m^{-1} K^{-1} at 800 K) due to the combination of a complex unit cell and large ADPs of the Ag and Rb ions. The high electrical resistivity and thermopower values are consistent with the valence electron count predicting than $Ag_3RbMo_9Se_{11}$ should be close to a semiconducting state. A maximum ZT value of 0.4 is reached at 800 K, indicating that substitutions on the Ag sites might provide a route to achieving good thermoelectric properties. Further investigations with other substituting elements on the Ag site would be of interest and may lead to enhanced thermoelectric performances and/or to novel crystal structures with different Mo_9Se_{11} cluster arrangement.

ASSOCIATED CONTENT

Accession Codes

CCDC 1550722 contains the supplementary crystallographic data for this paper. These data can be obtained free of charge via www.ccdc.cam.ac.uk/data_request/cif, or by emailing data_request@ccdc.cam.ac.uk, or by contacting The Cambridge Crystallographic Data Centre, 12 Union Road, Cambridge CB2 1EZ, UK; fax: +44 1223 336033.

AUTHOR INFORMATION

Corresponding Author

*E-mail: patrick.gougeon@univ-rennes1.fr.

ORCID

Patrick Gougeon: 0000-0003-4778-5581

Christophe Candolfi: 0000-0002-1248-5354

Notes

The authors declare no competing financial interest.

REFERENCES

(1) Goldsmid, H. J. In *Thermoelectric Refrigeration;* Temple Press Books Ltd: London, U.K., 1964.

(2) *Thermoelectrics and Its Energy Harvesting;* Rowe, D. M., Ed.; CRC Press: Boca Raton, FL, 2012.

(3) *Thermoelectrics Handbook: Macro to Nano;* Rowe, D. M., Ed.; CRC Press: Boca Raton, FL, 2006.

(4) Zhou, T.; Lenoir, B.; Colin, M.; Dauscher, A.; Al Orabi, R. A. R.; Gougeon, P.; Potel, M.; Guilmeau, E. Promising Thermoelectric Properties in $Ag_xMo_9Se_{11}$ Compounds ($3.4 \leq x \leq 3.9$). *Appl. Phys. Lett.* **2011**, *98*, 162106.

(5) Zhou, T.; Colin, M.; Candolfi, C.; Boulanger, C.; Dauscher, A.; Santava, E.; Hejtmanek, J.; Baranek, P.; Al Rahal Al Orabi, R.; Potel, M.; Fontaine, B.; Gougeon, P.; Gautier, R.; Lenoir, B. Comprehensive Study of the Low-Temperature Transport and Thermodynamic Properties of the Cluster Compounds $Ag_xMo_9Se_{11}$ ($3.41 \leq x \leq 3.78$). *Chem. Mater.* **2014**, *26*, 4765−4775.

(6) Al Rahal Al Orabi, R.; Gougeon, P.; Gall, P.; Fontaine, B.; Gautier, R.; Colin, M.; Candolfi, C.; Dauscher, A.; Hejtmanek, J.; Malaman, B.; Lenoir, B. X-ray Characterization, Electronic Band Structure, and Thermoelectric Properties of the Cluster Compound $Ag_2Tl_2Mo_9Se_{11}$. *Inorg. Chem.* **2014**, *53*, 11699−11709.

(7) Gougeon, P.; Gall, P.; Al Rahal Al Orabi, R.; Fontaine, B.; Gautier, R.; Potel, M.; Zhou, T.; Lenoir, B.; Colin, M.; Candolfi, C.; Dauscher, A. Synthesis, Crystal and Electronic Structures, and Thermoelectric Properties of the Novel Cluster Compound $Ag_3In_2Mo_{15}Se_{19}$. *Chem. Mater.* **2012**, *24*, 2899−2908.

(8) Al Rahal Al Orabi, R.; Fontaine, B.; Gautier, R.; Gougeon, P.; Gall, P.; Bouyrie, Y.; Dauscher, A.; Candolfi, C.; Lenoir, B. Cu Insertion Into the Mo_{12} Cluster Compound $Cs_2Mo_{12}Se_{14}$: Synthesis, Crystal and Electronic Structures, and Physical Properties. *Inorg. Chem.* **2016**, *55*, 6616−6624.

(9) Daigre, G.; Gougeon, P.; Gall, P.; Gautier, R.; Guillou, O.; Vaney, J.-B.; Candolfi, C.; Dauscher, A.; Lenoir, B. Synthesis, Crystal Structure and High-Temperature Transport Properties of the New Cluster Compound $Rb_2Mo_{15}Se_{19}$. *J. Solid State Chem.* **2016**, *237*, 1−6.

(10) Picard, S.; Gougeon, P.; Potel, M. $Rb_{10}Mo_{36}S_{38}$: A Novel Reduced Molybdenum Sulfide Containing the Highest Nuclearity Transition Metal Cluster in a Solid-State Compound. *Angew. Chem., Int. Ed.* **1999**, *38*, 2034−2036.

(11) Picard, S.; Saillard, J.-Y.; Gougeon; Noël, H. P.; Potel, M. $Rb_{2n}(Mo_9S_{11})(Mo_{6n}S_{6n+2})$ (n = 1 to 4): A Novel Family of Superconducting Molybdenum Cluster Compounds. *J. Solid State Chem.* **2000**, *155*, 417−426.

(12) (a) Gougeon, P.; Potel, M.; Padiou, J.; Sergent, M. Synthesis, Crystal Structure and Electrical Properties of the First Compound Containing Uniquely $Mo_{12}Se_{14}$ Cluster Units. *Mater. Res. Bull.* **1987**, *22*, 1087−1092. (b) Gautier, R.; Picard, S.; Gougeon, P.; Potel, M. Synthesis, Crystal and Electronic Structures, and Electrical Properties of $Rb_2Mo_{12}Se_{14}$ Containing Trioctahedral Mo_{12} Clusters. *Mater. Res. Bull.* **1999**, *34*, 93−101.

(13) (a) Gougeon, P.; Potel, M.; Sergent, M. Structure of $Rb_3Mo_{15}Se_{17}$ Containing the New Mo_{15} Clusters. *Acta Crystallogr.* **1989**, *C45*, 182−185. (b) Gougeon, P.; Potel, M.; Sergent, M. Structure of $Cs_3Mo_{15}Se_{17}$. *Acta Crystallogr.* **1989**, *C45*, 1413−1415.

(14) Gougeon, P.; Potel, M.; Padiou, J.; Sergent, M. $Rb_4Mo_{18}Se_{20}$ First Structural Type Containing the New $Mo_{18}Se_{20}$ Cluster Unit. *Mater. Res. Bull.* **1988**, *23*, 453−460.

(15) Picard, S.; Gougeon, P.; Potel, M. Single-Crystal Structure of $Cs_5Mo_{21}S_{23}$. *Acta Crystallogr.* **1997**, *C53*, 1519−1521.

(16) Gougeon, P. Nouveaux Chalcogénures Ternaires de Molybdène à Clusters Condensés Synthèses, Structures et Propriétés Physiques. Thesis, University of Rennes: France, 1984.

(17) Gougeon, P.; Padiou, J.; Le Marouille, J.-Y.; Potel, M.; Sergent, M. $Ag_{3.6}Mo_9Se_{11}$ Premier Composé à Clusters Mo_9 dans des Motifs Mo_9Se_{11}. *J. Solid State Chem.* **1984**, *51*, 218−226.

(18) Masschelein, P.; Candolfi, C.; Dauscher, A.; Al Rahal Al Orabi, R.; Gougeon, P.; Potel, M.; Gautier, R.; Lenoir, B. to be published.

(19) Colin, M.; Zhou, T.; Lenoir, B.; Dauscher, A.; Al Rahal Al Orabi, R.; Gougeon, P.; Potel, M.; Baranek, P.; Semprimoschnig, C. Optimization of Bulk Thermoelectrics: Influence of Cu Insertion in $Ag_{3.6}Mo_9Se_{11}$. *J. Electron. Mater.* **2012**, *41*, 1360−1364.

(20) Gougeon, P.; Potel, M.; Gautier, R. Syntheses and Structural, Physical, and Theoretical Studies of the Novel Isostructural Mo_9 Cluster Compounds $Ag_{2.6}CsMo_9Se_{11}$, $Ag_{4.1}ClMo_9Se_{11}$, and h-Mo_9Se_{11} with Tunnel Structures. *Inorg. Chem.* **2004**, *43*, 1257−1263.

(21) de Meulenaer, J.; Tompa, H. The Absorption Correction in Crystal Structure Analysis. *Acta Crystallogr.* **1965**, *19*, 1014−1018.

(22) Altomare, A.; Burla, M. C.; Camalli, M.; Cascarano, G. L.; Giacovazzo, C.; Guagliardi, A.; Moliterni, A. G. G.; Polidori, G.; Spagna, R. SIR97: a new tool for crystal structure determination and refinement. *J. Appl. Crystallogr.* **1999**, *32*, 115−119.

(23) Sheldrick, G. M. *SHELXL-97,* A program for crystal structure analysis; University of Göttingen: Göttingen, Germany, 1997.

(24) Petricek, V.; Dusek, M. *Jana2000;* Institute of Physics, Academy of Sciences of the Czech Republic: Prague, Czech Republic, 2000.

(25) Spek, A. L. J. Single-crystal structure validation with the program. *J. Appl. Crystallogr.* **2003**, *36*, 7−13.

(26) Rodriguez-Carvajal, J. *Phys. B* **1993**, *192*, 55−69.

(27) Salloum, D.; Gautier, R.; Gougeon, P.; Potel, M. Syntheses and Structural Trends of the $In_xMo_{15}S_{19}$ ($0 \leq x \leq 3.7$) Compounds Containing Mo_6 and Mo_9 Clusters. *J. Solid State Chem.* **2004**, *177*, 1672−1680.

DOI: 10.1021/acs.inorgchem.7b01200
Inorg. Chem. XXXX, XXX, XXX−XXX

(28) Schäfer, H.; Von Schnering, H. G. Metall-Metall-Bindungen bei Niederen Halogeniden, Oxyden und Oxydhalogeniden Schwerer Übergangsmetalle Thermochemische und Strukturelle Prinzipien. *Angew. Chem.* **1964**, *76*, 833−849.
(29) Aydemir, U.; Candolfi, C.; Ormeci, A.; Oztan, Y.; Baitinger, M.; Oeschler, N.; Steglich, F.; Grin, Yu. Low-temperature thermoelectric, galvanomagnetic, and thermodynamic properties of the type-I clathrate $Ba_8Au_xSi_{46-x}$. *Phys. Rev. B: Condens. Matter Mater. Phys.* **2011**, *84*, 195137.
(30) Suekuni, K.; Avila, M. A.; Umeo, K.; Takabatake, T. Cage-size control of guest vibrations and thermal conductivity in $Sr_8Ga_{16}Si_{30-x}Ge_x$. *Phys. Rev. B: Condens. Matter Mater. Phys.* **2007**, *75*, 195210.
(31) Bentien, A.; Nishibori, E.; Paschen, S.; Iversen, B. B. Crystal structures, atomic vibration, and disorder of the type-I thermoelectric clathrates $Ba_8Ga_{16}Si_{30}$, $Ba_8Ga_{16}Ge_{30}$, $Ba_8In_{16}Ge_{30}$ and $Sr_8Ga_{16}Ge_{30}$. *Phys. Rev. B: Condens. Matter Mater. Phys.* **2005**, *71*, 144107.
(32) Paschen, S.; Carrillo-Cabrera, W.; Bentien, A.; Tran, V. H.; Baenitz, M.; Grin, Yu.; Steglich, F. Structural, transport, magnetic, and thermal properties of $Eu_8Ga_{16}Ge_{30}$. *Phys. Rev. B: Condens. Matter Mater. Phys.* **2001**, *64*, 214404.
(33) Candolfi, C.; Aydemir, U.; Koza, M. M.; Baitinger, M.; Grin, Yu.; Steglich, F. Inelastic Neutron Scattering Study of the Lattice Dynamics in the Clathrate Compound $BaGe_5$. *J. Phys.: Condens. Matter* **2015**, *27*, 485401.
(34) Suekuni, K.; Kunii, M.; Nishiate, H.; Nishibori, E.; Maki, S.; Ohta, M.; Yamamoto, A.; Koyano, M. High-performance thermoelectric mineral $Cu_{12-x}Ni_xSb_4S_{13}$ tetrahedrite. *J. Appl. Phys.* **2013**, *113*, 43712.
(35) Lara-Curzio, E.; May, A. F.; Delaire, O.; McGuire, M. A.; Lu, X.; Liu, C.-Y.; Case, E. D.; Morelli, D. T. Low-temperature Heat Capacity and Localized Vibrational Modes in Natural and Synthetic Tetrahedrites. *J. Appl. Phys.* **2014**, *115*, 193515.
(36) Bouyrie, Y.; Candolfi, C.; Pailhès, S.; Koza, M. M.; Malaman, B.; Dauscher, A.; Tobola, J.; Boisron, O.; Saviot, L.; Lenoir, B. From Crystal to Glass-like Thermal Conductivity in Crystalline Minerals. *Phys. Chem. Chem. Phys.* **2015**, *17*, 19751−19758.
(37) Gautier, R.; Gougeon, P.; Halet, J.-F.; Potel, M.; Saillard, J.-Y. New experimental and theoretical studies on condensed molybdenum chalcogenide cluster compounds. *J. Alloys Compd.* **1997**, *262*−*263*, 311−315.
(38) Cahill, D. G.; Watson, S. K.; Pohl, R. O. Lower limit to the thermal conductivity of disordered crystals. *Phys. Rev. B: Condens. Matter Mater. Phys.* **1992**, *46*, 6131−6140.

DOI: 10.1021/acs.inorgchem.7b01200
Inorg. Chem. XXXX, XXX, XXX−XXX